Mixed-Precision Computing in the GRIST Dynamical Core for Weather and Climate Modelling

Siyuan Chen[1,5], Yi Zhang[1,3,5], Yiming Wang[1,5], Zhuang Liu[2], Xiaohan Li[2], Wei Xue[4]

1 2035 Future Laboratory, PIESAT Information Technology Co., Ltd., Beijing, China

2 Ministry of Education Key Laboratory for Earth System Modelling, Department of Earth System Science, Tsinghua University, Beijing, China

3 Chinese Academy of Meteorological Sciences, Beijing, China

4 Department of Computer Science and Technology, Tsinghua University, Beijing, China

5 Beijing Research Institute, Nanjing University of Information Science and Technology, Beijing, China

Correspondence to: Yi Zhang (zhangyi_fz@piesat.cn)

Abstract. Atmosphere modelling applications become increasingly memory-bound due to the inconsistent development rates between processor speeds and memory bandwidth. In this study, we mitigate memory bottlenecks and reduce the computational load of the GRIST dynamical core by adopting the mixed-precision computing strategy. Guided by a limited-degree of iterative development principle, we identify the equation terms that are precision insensitive and modify them from double- to single-precision. The results show that most precision-sensitive terms are predominantly linked to pressure-gradient and gravity terms, while most precision-insensitive terms are advective terms. The computational cost is reduced without compromising the solver accuracy. The runtime of the model's hydrostatic solver, non-hydrostatic solver, and tracer transport solver is reduced by 24%, 27%, and 44%, respectively. A series of idealized tests, real-world weather and climate modelling tests, has been performed to assess the optimized model performance qualitatively and quantitatively. In particular, in the high-resolution weather forecast simulation, the model sensitivity to the precision level is mainly dominated by the small-scale features. While in long-term climate simulation, the precision-induced sensitivity can form at the large scale.

1 Introduction

Increasing model resolution is an effective approach of enhancing the atmosphere model forecast accuracy (Bauer et al. 2021; Benjamin et al.2019; Yu et al. 2019). Highly accurate, efficient, stable and scalable global dynamical cores have been widely pursued over the past two decades (e.g., Tomita and Satoh 2004; Harris and Lin 2012; Skamarock et al. 2012; Zängl et al. 2015; Wedi et al. 2020; Sergeev et al. 2023; Zhang et al. 2023). Doubling the horizontal resolution with a fixed vertical resolution leads to an increase of computational amount by a factor of ~2^3, a significant challenge in terms of computational cost and energy consumption.

Operational weather and climate forecasting is a field where the dual demands of accuracy and computational efficiency converge, necessitating both quality and speed. In the context of high-resolution meso-scale forecasting, which operates on

30 scales of a few kilometers, computational efficiency itself implies forecast accuracy. Faster models enable more frequent
forecast-assimilation cycles and the use of larger ensemble sizes within the constraints of finite computational resources. To
tackle these computational hurdles, efforts have concentrated on enhancing the efficiency of numerical models. Progress
such as Field Programmable Gate Arrays (FPGAs) and heterogeneous computing (e.g., Gan et al. 2013; Yang et al. 2016; Fu
et al. 2017; Gu et al. 2022; Taylor et al. 2023), alongside compiler optimizations (e.g., Santos et al. 2024), have

35 demonstrated significant potential in accelerating earth system model.

Conventional weather/climate model development has typically relied on double-precision (64-bit) floating-point. The
transition from double- to single-precision (32-bit) or even half-precision floating-point arithmetic presents an intriguing
avenue for enhancing the computational efficiency (Düben et al. 2014). Single-precision computation unveils several
compelling advantages, especially when confronted with the memory wall (Abdelfattah et al. 2021; Fornaciari et al. 2023;

40 Brogi et al. 2024). Beyond the alleviation of memory constraints, single-precision arithmetic promises three distinct benefits:
accelerated arithmetic operations, improved cache hit rates, and reduced inter-node data communication (Baboulin et al.
2009; Düben and Palmer 2014; Düben et al. 2015; Váňa et al. 2016; Nakano et al. 2018). The benefits highlighted illustrate
the capability of single-precision computation to boost computational efficiency in high-performance computing tasks,
especially within the realm of large-scale weather and climate simulations where computational expenses are significant.

45 However, a wholesale migration from double- to single-precision computing may not always yield beneficial outcomes.
This has led to the exploration of precision sensitive model component and/or physical scale in earth system modeling (e.g.,
Thornes et al. 2017; Nakano et al. 2018; Chantry et al. 2019; Maynard and Walters 2019; Cotronei and Slawig 2020). Single-
precision algorithms may struggle to converge or achieve the required precision when tackling intricate fluid dynamics
simulations. In certain scenarios, single-precision computations can also result in floating-point under/overflow (Váňa et al.

50 2016; Cotronei et al. 2020). Additionally, physical parameterization schemes in the atmospheric models may amplify the
grid-scale oscillations when executed in a pure single-precision mode (Váňa et al. 2016). Therefore, it becomes imperative to
identify the specific algorithms within the modeling framework that are sensitive to the precision level.

Previous studies have made a notable progress. A pivotal study (Váňa et al. 2016) explored the reduction of almost all
real-number variables in the Integrated Forecast System (IFS) of the European Center for Medium-Range Weather

55 Forecasting (ECMWF) from 64 bits to 32 bits. Results revealed that reducing precision did not significantly compromise the
model accuracy, while it considerably reduced the computational burden by a factor of ~40%. Based on the dynamical core
of the nonhydrostatic icosahedral model (NICAM), Nakano et al. (2018) witnessed an undesirable wavenumber-5 structure
when completely using single-precision computing. This abnormal wave growth was traced back to the errors in the grid cell
geometry calculations. By using double precision for only necessary parts in the dynamical core and single precision for all

60 other parts, the model successfully simulated the baroclinic wave growth, and achieved a ~46% reduction of runtime. Based
on the Yin-He global spectral model, Yin et al. (2021) used a single-precision fast spherical harmonic transform (SHT) to
conduct a 10-day global simulation and a 30-day retrospective forecasting experiment. Their simulations reproduced the

major precipitation events over southeastern China. The single-precision fast SHT may lead to a reduction of runtime by ~25.28% without significantly affecting the forecasting skill. Cotronei et al. (2020) converted the majority of the

65 computations within the radiation component of European Centre Hamburg Model (ECHAM) to single-precision, resulting in a 40% reduction in the runtime of the individual component. The obtained results were comparable to those achieved with double-precision. Banderier et al. (2023) indicated that employing single precision for regional climate simulations can significantly reduce computational costs (~30%) without significantly compromising the quality of model results.

While these studies have demonstrated various ways for precision optimization, certain limitations remain. First, some

70 studies focused on a complete transition to single-precision, potentially overlooking the precision-sensitive components and lacked a discussion of optimization strategies. Moreover, the applicability of mixed-precision in global climate simulations remains to be validated. Furthermore, because of the diversity of numerical models and algorithms, encompassing grid systems and solver techniques, these differences may lead to the model-specific precision sensitivity. Certain algorithms may remain amenable to single-precision computations, while others necessitate the use of double precision for stability and

75 accuracy. These gaps in the literature underscore the need for the present research to explore precision sensitivity, and to test the reduced-precision computing for both weather and climate simulations.

In this study, we explored the strategies of mixed-precision computing in the dynamical core of the Global-Regional Integrated Forecast System (GRIST; Zhang et al. 2019; Zhang et al. 2020). GRIST is a unified weather-climate model system designed for both research and operational modeling applications. Through a detailed implementation by modifying

80 certain parts of the original (double-precision) dynamical core to support single-precision, a significant reduction of the computational burden has been achieved without sacrificing the solution accuracy, stability, and physical performance. This has been validated based on a series numerical tests ranging from idealized to real-world flow.

The remainder of this paper is organized as follows. Section 2 introduces the GRIST model, presents the mixed-precision optimization strategies, code modifications and highlighting the key equation terms sensitive to precision. Section

85 3 examines the computational performance of mixed-precision computing. Section 4 evaluates the physical performance of mixed-precision computing in a series of test cases. A summary is given in Section 5.

2.1. GRIST

The GRIST dynamical core employs layer-averaged governing equations based on the generalized hybrid sigma-mass vertical coordinate and a horizontal unstructured grid, allowing a switch between the hydrostatic and non-hydrostatic solvers

90 (Zhang 2018; Zhang et al. 2019; Zhang et al. 2020). Prognostic variables are arranged in a hexagonal Arakawa-C grid approach. The hydrostatic solver is fully explicit, based on the Runge-Kutta integrator and the Mesinger forward-backward scheme. The nonhydrostatic solver employs a horizontally explicit vertically implicit approach. There is no time splitting in the integration of the dry dynamical core (dycore hereafter), while the tracer transport module is time-splitted from the dycore, and supports several transport schemes for various applications (Zhang et al. 2020). In this study, a third-order

95 upwind flux operator combined with the Flux-Corrected Transport limiter is used in the horizontal, and an adaptively implicit method is used in the vertical (cf., Li and Zhang 2022).

2.2 Mixed-precision optimization strategy

The purpose is to decrease the precision level (and thus computational cost) and maintain the accuracy and stability. Before implementing mixed-precision computing, we have checked that completely using single precision for the entire

100 dynamical core leads to an unacceptable accuracy loss (see Section 4.1). However, considering the extensive codebase and its degree of complexity, comprehensively and randomly testing every component and variable is impractical. An iterative development approach with a minimum degree of trial and error is used to identify the model components that are sensitive to the precision level. The dry baroclinic wave of Jablonowski and Williamson (2006) is used as a benchmark test during the iterative development cycle because this case has complex fluid dynamics characteristics and is very sensitive to numerical

105 precision.

We established an acceptable error threshold, α, to assess whether the difference between outcomes from double-precision and mixed-precision simulations falls within a tolerable limit. Results from original double-precision computing serve as the true values. The iteration is: initially, a 10-day simulation was executed. We then embarked on a series of precision reduction tests for selected model variables, and we computed the error norm of two diagnostic variables for each

110 test. E is defined to represent the overall error level:

$$E = \max\big(L(ps), L(vor)\big) \tag{1}$$

$$L(x) = \max\big(L_1(\mathcal{H}), L_2(\mathcal{H}), L_\infty(\mathcal{H})\big) \tag{2}$$

where L_1, L_2, and L_∞ represent the first, second and infinite norm of variable $\mathcal{H}$. ps is surface pressure and vor is relative vorticity. These two variables are selected as our benchmark diagnostic metrics because they can effectively quantify

115 deviations in the mass field and velocity field. Should "error" E exceed α (0.05 for this study), the modification is deemed unacceptable and consequently abandoned; otherwise, the modification is accepted, allowing a further reduction in variable precision based on this new configuration. Please note that the precision optimization tests were conducted using the G8 grid. The grid names and their corresponding resolutions can be found in Table 1.

Technically, the switch between double-precision and single-precision code is defined through the FORTRAN KIND

120 parameter, specified in a constant module. As single-precision results may not always replicate the double-precision results and can occasionally generate unacceptable errors (e.g., see Section 3.2), it is crucial to identify precision-sensitive variables and solver components. An additional parameter 'ns' has been introduced in this constant module for the precision-insensitive variables. This modification facilitates the transition between double-precision, single-precision, and mixed-precision computations. Please note that only the subroutine of the solver is modified, indicating that the model initialization

125 section remains in double-precision operations. If the solver requires single-precision operands, double-precision variables need to be converted to single-precision after initialization. This method ensures a streamlined transition to mixed precision with minimal changes to the code structure.

Some important aspects are summarized as follows:

(i)   Model variables insensitive to the precision level are set to the type parameter "ns". When "ns" is defined as single
130   precision, the code executes mixed-precision computations; when defined as double precision, the code regresses
        double-precision computing and produces identical solutions as the original unmodified code;

(ii)   Appropriately decompose computations involving implicit type conversions to reduce performance degradation due
        to precision conversion. For instance, 'a = b * c'. Here, 'a' is a single-precision floating point, 'b' a larger double-
        precision float, and 'c' a single-precision float. The conversion of 'c' to double-precision can introduce extra
135   rounding errors. These errors, amplified by 'b', may accumulate over time, adversely affecting model outcomes.
        Single-precision calculations provide a consistent error boundary, unlike mixed-precision which introduces
        uncertainty. In some cases, results might even be better if the computation of a function were entirely in single
        precision. Hence, optimization should proceed with caution, considering these error dynamics.

(iii)   The Message Passing Interface (MPI) communication was modified for single-precision variables; The built-in
140   functions such as 'HUGE' or 'TINY' are used to obtain very large or very small values respectively, to ensure the
        values fall within the precision range of the variables.

2.3 Mixed-precision optimization results

Following the strategy outlined in Section 2.2, the mixed-precision GRIST dynamical core is established. The
optimization results are summarized based on the continuous-form governing equations:

$$\frac{\partial(\pi_s - \pi_t)}{\partial t} + \boxed{\int_{\eta_t}^{\eta_s} \nabla \cdot (\delta\pi \boldsymbol{V}) d\eta} = 0 \tag{3}$$

$$\frac{\partial(\delta\pi\theta_m)}{\partial t} + \nabla \cdot (\delta\pi\boldsymbol{V}\theta_m) + \delta\left(\frac{\partial\pi}{\partial\eta}\dot{\eta}\theta_m\right) = \delta\pi S(\theta_m) \tag{4}$$

$$\frac{\partial u_n}{\partial t} + \zeta_p \delta\pi u_t + \boxed{\frac{\partial KE}{\partial n}} + \boxed{\dot{\eta}\frac{\partial u_n}{\partial\eta}} = \mathcal{L}\boxed{\left[-\frac{1}{\rho_d}\frac{\partial p}{\partial n} - \frac{\delta p}{\delta\pi}\frac{\partial\phi}{\partial n}\right]} + S(u_n) \tag{5}$$

$$\frac{\partial w}{\partial t} + \boldsymbol{V}\cdot\nabla w + \dot{\eta}\frac{\partial w}{\partial\eta} = \mathcal{L}g\overline{\frac{\partial p}{\partial\pi}} - g + S(w) \tag{6}$$

$$\frac{\partial\phi}{\partial t} + \boldsymbol{V}\cdot\nabla\phi + \dot{\eta}\frac{\partial\phi}{\partial\eta} = \overline{wg} + S(\phi) \tag{7}$$

$$\frac{\partial\phi}{\partial\pi} = -\alpha_d \tag{8}$$

$$p = p_0\left(-\frac{R_d\delta\pi\theta_m}{p_0\delta\phi}\right)^{\gamma} \tag{9}$$

$$\frac{\partial(\delta\pi q_i)}{\partial t} + \nabla\cdot(\delta\pi\boldsymbol{V}q_i) + \delta\left(\frac{\partial\pi}{\partial\eta}\dot{\eta}q_i\right) = \delta\pi S(q_i) \tag{10}$$

The meaning of each variable in the equations *exactly* follows Zhang et al. (2020) so that we avoid repeating
explanation. Model variables in red denote single-precision operands, variables in black represent double-precision operands.

155 Black boxes indicate that this part uses double-precision variables for computation, but the tendency is saved as single precision. Green indicates that this variable is diagnosed mostly from single-precision variables. Specifically, $\zeta_p = \frac{\zeta_a}{\delta\pi}$ is highly sensitive to the precision of $\delta\pi$, requiring a double precision $\delta\pi$.

For the dycore, the precision sensitivity varies among different terms. The precision-sensitive terms are primarily related to pressure gradient and gravity terms. The precision-insensitive terms are mainly advective, which may tolerate
160 lower numerical precision. Computationally, the advective parts of the equations are using higher-order operators which are responsible for the major computational burden. The passive tracer transport equation (Eq. 10) can be mostly computed using single precision. The only part needs a careful modification is the blue part, which indicates that it uses single-precision variables for computing, but the result is saved as double precision. $\delta\pi V$ (representing the mass flux) in Eq. (10) is accumulated and averaged from $\delta\pi V$ in Eq. (3), so computing it uses single precision. But when using it for tracer transport,
165 this variable is converted to double precision so that the mass continuity equation of tracer transport uses a double-precision mass flux.

The mass continuity equation Eq. (3) is solved using a flux form, ensuring global mass conservation of $\pi_s - \pi_t$ (π_t is a constant) within the bounds of machine rounding errors, which is at the double-precision level. Using single precision $\delta\pi V$ implies that mass continuity is locally conserved at the single precision level. Recognizing the potential importance of local
170 mass conservation (e.g., Thuburn 2008), a compilation switch is designed, so that approximating $\delta\pi V$ and the related mass continuity tendency can be achieved in either single-precision or double-precision. The time difference between approximating the continuity equation using single-precision and double-precision accounts for ~1% -2% of the total computational time. We will examine the model sensitivity to this operation in Section 4.4.

3 Computational performance

175 Before showing the physical performance, we first examine the computational performance of the optimized dynamical core. All computing performance are carried out on a local supercomputing cluster. Each computing node is equipped with 128GB memory, and the Central Processing Unit (CPU) is a Hygon C86 7285 model at 2.0 GHz. Each CPU features a 32 KB L1 data cache, a 64 KB L1 instruction cache, a 512 KB L2 cache, and an 8192 KB L3 cache. We use "SGL" to denote pure single precision computing, "DBL" to denote pure double precision, and "MIX" to represent mixed precision computing.
180 All experiments were conducted on a G8 grid, submitted with the same topology: 756 MPI tasks distributed across six nodes.

Compared to the double-precision model, the runtime of the mixed-precision model for the non-hydrostatic dry dynamical core (NDC), hydrostatic dry dynamical core (HDC) and tracer transport solver reduced by 27% (24%) and 44% (Table 2). The runtime of the mixed-precision dycore solver is still larger compared to the single-precision dycore, indicating the time overhead incurred by the use of double-precision in precision-sensitive algorithms. The runtime of the mixed-
185 precision tracer transport solver is comparable to that of the single-precision tracer transport solver, as most computations in

the tracer transport module now use single-precision computing. It should be noted that the time gains from mixed-precision computing may also depend on hardware and compiler options (e.g., Brogi et al. 2024). This is out of the scope of this study.

4 Physical Performance

Due to the inherent complexity of atmosphere models, which have dycore, tracer transport, and model physics suites, 190 directly assessing errors induced by precision in the real cases is not precise. To ensure robustness, a hierarchy of five test cases from simple to complex is adopted for model evaluation.

4.1 Moist baroclinic wave

This case is from the DCMIP2016, as outlined by Ullrich et al. (2014), a modified approach to the dry baroclinic instability scenario (Jablonowski and Williamson 2006). This experimental setup triggers the emergence of an unstable 195 baroclinic wave pattern, initiated by early perturbations, which exhibits exponential growth and attains its maximum intensity around the 11th day. The experiment incorporates a passive tracer representing water vapor, which is subject to passive advection. Although the mixing ratio marginally influences the pressure gradient force, as noted by Zhang et al. (2020), the overall behaviour of wave growth is in substantial agreement with that in the dycore (Zhang et al. 2019). The primary objective is to assess the model's efficacy in replicating the typical dynamics of moist atmospheric conditions across 200 various precision settings.

Figure 1 shows surface pressure and relative vorticity field at the model level near 850hPa at day 11, as simulated by the G8 resolutions. The baroclinic waves shown the anticipated growth in the DBL simulation (Figs. 1a). In the SGL simulation, the primary growth fluctuations in the DBL simulation were reproduced (Figs. 1c). However, in the Northern Hemisphere, there were developments of incorrect spurious waves, whose intensity was comparable to the major fluctuations 205 (Figs. 1c). The Southern Hemisphere exhibited a weaker structure of spurious waves (Figs. 1c). The results from the MIX simulation displayed patterns much closer to those in the DBL simulation (Figs. 1e).

The primary difference between MIX and DBL simulations lies in the vicinity of strong gradients along the cold front (Figs. 1c). But the primary fluctuations in both MIX and DBL simulations exhibit a high degree of similarity in their patterns (Figs. 1a and 1e), indicating that precision levels have a tangible impact on the phase speed of wave propagation.

210 The error introduced by SGL and MIX can be quantified by comparing solutions to a DBL solution. Following Jablonowski and Williamson (2006), l_2 error norms of the relativity vorticity field are compared on the global grid as a function of time. Figure 2 shows the l_2 norm for the SGL and MIX. In the initial stages of the model integration, the errors in the SGL simulations increased rapidly. By checking the original fields (figure not shown), it was found that numerous small-scale spurious fluctuations had emerged on both sides of the equator, the intensity of which was similar to the physically 215 meaningful fluctuations.

After day 6, the primary fluctuations of the baroclinic waves in the SGL simulations began to develop, resembling the behaviour of the DBL simulations, and the errors started to decrease (Fig. 2). By day 10, the fluctuations rapidly developed, the primary fluctuations grew robustly, and the spurious fluctuations produced in the early stages of the SGL simulations

also rapidly developed, leading to an increase in errors (Fig. 2). On day 11, the intensity of the spurious fluctuations developed in SGL was close to that of the primary fluctuations, which is unacceptable. Due to the slow growth of the primary fluctuations in the early stages, the MIX simulation exhibited minimal errors before day 9 (Fig. 2). Subsequently, as the fluctuations matured rapidly, prominent differences in phase speed compared to the DBL emerged, leading to a rapid increase in errors.

4.2 Splitting supercell thunderstorms

The splitting supercell test of DCMIP2016 (Klemp et al. 2015; Zarzycki et al. 2019) emphasizes the importance of scrutinizing non-hydrostatic model simulations of small-scale dynamics, especially as models approach spatial resolutions on the (sub) kilometre scale. This test utilized the small-planet testing framework (Wedi and Smolarkiewicz 2009), a cost-effective approach by scaling down Earth's radius by a factor of 120. The model employs the Kessler warm-rain microphysics scheme for simplified physics. This particular test case is characterized by unstable atmospheric conditions conducive to moist convection, posing a challenge numerical accuracy and stability. Klemp et al. (2015) suggested that an increase in horizontal resolution should lead to convergent solutions. For GRIST, this behaviour has been verified by Zhang et al. (2020). Our investigation further examines the capability of the MIX configuration to accurately replicate the behaviours observed in the DBL simulations.

Figure 3 shows the q_r mixing ratio at 5 km elevation in both DBL and MIX simulations at three resolution choices (G6: ~1km, G7: ~0.5km and G8: ~0.25km). The DBL and MIX solutions show bulk similarities across all the resolutions. At 7200s, a single updraft splits and evolves into a symmetric storm propagating towards the poles, with two supercells located ~30° from the equator. These supercells show subtle differences in their structure and intensity. The differences in the structure of the supercells are larger at lower resolutions than at higher resolutions. In the MIX simulation at 1 km, an additional small-scale local maximum is present near the storm core on the north side of the Equator (Figs. 3d). The MIX simulated rainfall intensity is slightly weaker than the DBL solutions in some configurations (Figs. 3b and 3e). As the resolution increases, the differences between MIX and DBL diminish (Figs. 3g, 3h and 3i).

Figure 4 shows the maximum vertical speed and area-integrated rainfall rate over the global domain as a function of time for each resolution. The vertical speed in both MIX and DBL increases with resolution (Figs. 4a). From the start of the model integration until 5400s, the vertical speed curves of MIX and DBL simulations nearly overlap (Figs. 4a). After 5400s, a noticeable deviation appears. The difference in vertical speed between MIX and DBL is minimal at 0.25 km resolution, while it is larger at 1 km and 0.5 km resolutions (Figs. 4a). The area-integrated rainfall rate curves exhibit similar evolutionary features (Figs. 4b). At a higher resolution of 0.25 km, the overall behaviour of supercells in MIX simulations is closer to that of DBL compared to 0.5km and 1 km resolutions. Both MIX and DBL solutions demonstrate good convergence.

4.3 Idealized tropical cyclone

This idealized tropical cyclone scenario integrates a three-dimensional dynamical core with a simple physics suite (Reed and Jablonowski 2012), alongside an analytic vortex initialization technique (Reed and Jablonowski 2011). The

experiment produces the evolution of a tropical cyclone from a nascent, idealized vortex, highlighting the model's sensitivity to various parameter adjustments. Notably, alterations in tracer transport schemes in GRIST can produce subtle sensitivities in the development of the tropical cyclone due to the pressure gradient terms (Zhang et al. 2020), thereby establishing this case useful for assessing model precision sensitivity.

Figure 5 displays the wind speed at day 10 for the DBL (Figs. 5a and 5b) and MIX (Figs. 5c and 5d) simulations at G8 resolution. Figure 5 (left) shows the longitude-height cross sections of the magnitude of the wind through the centre latitude of the vortex. Figure 5 (right) displays the horizontal cross sections of the magnitude of the wind at surface model layer. The centre of vortex is defined as the grid point with the minimum surface pressure. At the day 10, the developed storm resembled a tropical cyclone. The overall behaviour in the MIX simulation was similar to that in the DBL simulation, with maximum winds near the surface and a distinct eyewall structure (Fig. 5). However, there was some differences in the vertical structure and centre location of the cyclone (Figs. 5a and 5c). In the MIX simulation, the generated cyclone was stronger, with higher wind speeds near the surface (Fig. 5c). The eyewall of the cyclone in the MIX simulation appeared less pronounced compared to that in the DBL simulation, where the cyclone's eyewall is narrower and straighter (Fig. 5c). Overall, the characteristics of the cyclone were comparable between the MIX and DBL simulations.

In addition to two deterministic control simulations using both double-precision and mixed-precision with the non-hydrostatic solver, eight ensemble simulations with the double-precision non-hydrostatic solver are further performed. This assesses the MIX simulation within the uncertainty range of the DBL simulation. The uncertainty range is quantified by the ensemble simulations encompassing eight initial-value perturbation members. Random small-amplitude perturbations were applied to the initial wind speeds (e.g., Li et al. 2020), where perturbations to the normal velocity at cell edges were prescribed within a range of 2% of their values in the control experiment.

Figure 6 describes the tracks of tropical cyclones, along with the evolution of minimum surface pressure and maximum surface wind speed over time. The red and blue lines represent two deterministic simulations conducted using MIX and DBL solvers, respectively. The eight random perturbation simulations with DBL solver are represented by gray lines. Minimal spread is observed in the early stages of the simulations (Figs. 6). Cyclone track separation between MIX and DBL simulations occurs at the day 1 (Fig. 6a). Subsequently, spread in the simulations increases over time (Figs. 6). The evolution of minimum surface pressure and maximum surface wind speed over time exhibits similar trends (Figs. 6b and 6c). No discernible difference is found between the sensitivity introduced by the MIX and that introduced by perturbed initial values in the DBL simulations. The overall behaviour of the MIX simulation falls within the range of uncertainty of the DBL simulation.

4.4 Atmospheric Model Intercomparison Project (AMIP) simulation

Following the establishment of the MIX dynamical core, a detailed examination of its integration with the model physics suite (Li et al. 2023) becomes crucial. The nonlinear interactions between the model's dynamics and its physical processes can result in varied performances across weather and climate simulations. It's imperative to investigate these differences to ensure that MIX simulations can accurately mirror the outcomes of DBL simulations in practical applications.

In assessing a new formulation for real-world modelling, our guiding principle is to first run long-term AMIP simulations (Zhang et al. 2021). This ensures that the model can achieve statistical equilibrium, maintain a realistic model climate, and has good integral properties such as conservation and balanced budgets (e.g., Fu et al. 2024). Subsequently, the

290 same model, with minimal application-specific modifications, undergoes shorter-range but higher-resolution, kilometre-scale tests (Zhang et al. 2022).

The AMIP experiment is conducted in alignment with Zhang et al. (2021). This involved running both global hydrostatic and non-hydrostatic models with the weather physics suite at a G6 over a decade, spanning from 2001 to 2010. The simulations were performed under conditions with prescribed climatological sea surface temperatures and sea ice

295 concentrations. The focus was narrowed to precipitation, which is a comprehensive metric due to its sensitivity to both model dynamics and physics, effectively reflecting the non-linear interactions that are crucial for accurate weather and climate simulations (Zhang and Chen 2016).

Figure 7 shows the simulated climatological (2001-2010) precipitation field for June-July-August (JJA) and December-January-February (DJF). Both the MIX hydrostatic and non-hydrostatic solvers are capable of replicating the JJA and DJF

300 precipitation patterns in the DBL simulations. The discrepancies between MIX and DBL simulations are similar in both hydrostatic and non-hydrostatic simulations, with the primary differences occurring in the tropics. The precipitation differences shift from north to south along with the main rain bands as the season transition from summer to winter. The deviation in summer precipitation is greater than that in winter precipitation, because convective activities are most vigorous. In the summer, the MIX simulation overestimates the precipitation in the tropical coastal regions of the Western Pacific,

305 especially along the western coast (Figs. 7a and 7b). In winter, the main biases in the MIX simulation are concentrated in the Southern Ocean (Figs. 7c and 7d).

These results may have two implications. In MIX simulations, the cumulative effects of rounding errors might be progressively magnified over the course of long-term climate integrations. This phenomenon could lead to notable differences in the simulated large-scale atmospheric phenomena. This contrasts with high-resolution shorter-range weather

310 modeling, where discrepancies primarily emerge at the small scales, as will be discussed in Section 4.5. This might imply that MIX may more diverge from their DBL counterparts over extended integration periods, necessitating a careful consideration of how rounding errors accumulate and their impact on the climate simulation performance.

Second, the differences induced by varying levels of precision can be further exacerbated by physical processes within the climate system. A clear example is observed in the tropical regions during the boreal summer, where higher

315 discrepancies are noted. This suggests that certain atmospheric conditions or regions, such as the tropics during periods of intense solar heating, may be more susceptible to the effects of precision-level differences. These conditions can amplify the inherent precision differences, leading to more pronounced variations.

In the MIX implementation, Eq. 3 implies that global mass is conserved at the double precision level. The local mass flux is only conserved at the single precision level, because the mass flux and its divergence are treated as single precision.

320 As mentioned in Section 2.3, we have retained a capability to compute the terms related to the mass flux divergence equation

also in the double precision. Local mass can be conserved at the double precision level as well. We then evaluated the long-term climate integration results based on the hydrostatic solver.

Figure 8 shows the differences of the climatological precipitation field between MIX with single- (MIX_SGL_mass) and double-precision (MIX_DBL_mass) mass flux divergence against the pure DBL simulation. In the summer, the simulation differences between the MIX_SGL_mass and MIX_DBL_mass solver for the continuous equations is small (Figs. 8a and 8b). In the winter, the deviations in the MIX_SGL_mass is smaller than those in the MIX_DBL_mass solver (Figs. 8c and 8d). The deviations are most pronounced in the tropical convective precipitation over the Southern Ocean (Figs. 8c and 8d). The larger difference between MIX_DBL_mass and DBL is *likely* due to implicit type conversions, as discussed in Section 2.2.

4.5 A global storm-resolving simulation

Under the constraints of today's computational resources, executing global storm-resolving nonhydrostatic simulations remains resource intensive (Satoh et al. 2017; Stevens et al. 2019). The use of MIX simulations presents a cost-effective solution to this challenge. However, it has been reported, for instance by Nakano et al. (2018), that as the resolution of the model increases, the difference between MIX and DBL may increase, especially for the smaller-scale flow features. This observation prompts a closer investigation into the performance of nonhydrostatic models at high-resolution modelling.

A global storm-resolving experiment at 5 km (G9B3) is performed using the MIX nonhydrostatic model, following Zhang et al. (2022). The model was integrated from UTC00, 10th, to UTC00, 15th, July, 2015. We expect that the developed mixed-precision dynamical core can replicate the behaviour of DBL in kilometre-scale weather simulations.

Figure 9 show the period-accumulated precipitation (UTC00, 10th-UTC23, 15th, 2015) from the MIX and DBL model runs. All data have been interpolated to the $0.5°$ regular latitude-longitude grid. The precipitation pattern simulated by MIX are very close to those of DBL simulations. MIX obtains nearly the same general position, orientation, and intensification of the rain band (Figs. 9a, 9b). MIX and DBL also produced very comparable kinetic energy spectra (figure not shown).

Like the AMIP simulations, the differences in precipitation are primarily located within the tropics, with the most pronounced differences in areas with vigorous convection. Close-ups of these locations reveal that it is small-scale (a few grid spacing) that is most sensitive to the precision level, because small scales are most sensitive to numerical discretization and dissipation (Jablonowski and Williamson 2011). Considering that global meso-scale forecast at a few kilometres would greatly benefit from ensemble prediction (Palmer 2019), in practice, the MIX induced small-scale sensitivity may also fall within the uncertainty range of the ensemble, similar to that in Section 4.3.

5 Summary

In this study, we investigated mixed-precision computing within the GRIST dynamical core, identifying the equation terms particularly sensitive to numerical precision. We outlined an optimization procedure characterized by a limited extent of iterative development. Given the current development trajectory of high-performance computing, where advancements in

memory bandwidth lag behind peak processor performance improvements, mixed-precision computation holds promise for enhancing weather and climate model development. The major conclusions are summarized as follows.

355   We discovered that terms sensitive to numerical precision primarily involve pressure gradient and gravity. In contrast, advective terms exhibit resilience to single precision and can be optimized. The advective terms are computationally more expensive than the pressure gradient and gravity terms. The viability of employing mixed-precision computing in the GRIST dynamical core has been validated across a spectrum of scenarios, from idealized flow to real-world AMIP and global storm-resolving simulations. These MIX experiments yielded results remarkably similar to those from DBL simulations. For

360 dycore, the runtime for hydrostatic and non-hydrostatic solvers was reduced by 24% and 27%, respectively. The tracer transport solver witnessed a runtime reduction of 44%. The overall time savings depend on the proportion of dycore and tracer transport in the total computation time, varying by application.

      We noted a higher sensitivity to precision in long-term climate simulations compared to short-term higher-resolution weather forecasts, particularly affecting the precipitation field over certain regions. In weather forecast, the difference

365 between MIX and DBL are mainly for the small scales, while in AMIP simulations, the difference is found for the larger scales. These effects may primarily stem from the model sensitivity to the precision level or from biases introduced by mixed-precision computations themselves.

      It also needs to recognize that while the mixed-precision GRIST dynamical core has been examined across multiple scenarios, more realistic tests and some fine tuning may still be needed to ensure robust operational forecasting. Some

370 alternative advection schemes in the tracer transport module have not been implemented to single precision yet and this can be achieved in future. The optimization and evaluation strategies can be reused.

Acknowledgments

Editors and reviewers are thanked for their handling and comments of this paper. This study is supported by a National Talent Project (2021).

375 **Code and Data availability**

Model code and plotting data related to this manuscript is available at: https://doi.org/10.5281/zenodo.10910354.

Author contribution

SYC developed the mixed precision model code and prepared the initial draft. YZ designed and led this model development research. YW contributed to experiments. All the authors discussed this work and contributed to the final manuscript version.

380 **Competing interests**

None.

References

Abdelfattah, A., Anzt, H., Boman, E. G., Carson, E., Cojean, T., Dongarra, J., Fox, A., Gates, M., Higham, N. J., Li, X. S., Loe, J., Luszczek, P., Pranesh, S., Rajamanickam, S., Ribizel, T., Smith, B. F., Swirydowicz, K., Thomas, S., Tomov, S., Tsai, Y. M., and Yang, U. M.: A survey of numerical linear algebra methods utilizing mixed-precision arithmetic, The International Journal of High Performance Computing Applications, 35, 344-369, doi:10.1177/10943420211003313, 2021.

Baboulin, M., Buttari, A., Dongarra, J., Kurzak, J., Langou, J., Langou, J., Luszczek, P., and Tomov, S.: Accelerating scientific computations with mixed precision algorithms, Computer Physics Communications, 180, 2526-2533, doi:https://doi.org/10.1016/j.cpc.2008.11.005, 2009.

Bauer, P., Dueben, P. D., Hoefler, T., Quintino, T., Schulthess, T. C., and Wedi, N. P.: The digital revolution of Earth-system science, Nature Computational Science, 1, 104-113, doi:10.1038/s43588-021-00023-0, 2021.

Benjamin, S. G., Brown, J. M., Brunet, G., Lynch, P., Saito, K., and Schlatter, T. W.: 100 Years of Progress in Forecasting and NWP Applications, Meteorological Monographs, 59, 13.11-13.67, doi:10.1175/AMSMONOGRAPHS-D-18-0020.1, 2019.

Brogi, F., Bnà, S., Boga, G., Amati, G., Esposti Ongaro, T., and Cerminara, M.: On floating point precision in computational fluid dynamics using OpenFOAM, Future Generation Computer Systems, 152, 1-16, doi:https://doi.org/10.1016/j.future.2023.10.006, 2024.

Chantry, M., Thornes, T., Palmer, T., and Düben, P.: Scale-Selective Precision for Weather and Climate Forecasting, Monthly Weather Review, 147, 645-655, doi:https://doi.org/10.1175/MWR-D-18-0308.1, 2019.

Cotronei, A. and Slawig, T.: Single-precision arithmetic in ECHAM radiation reduces runtime and energy consumption, Geosci. Model Dev., 13, 2783-2804, doi:10.5194/gmd-13-2783-2020, 2020.

Düben, P. D., McNamara, H., and Palmer, T. N.: The use of imprecise processing to improve accuracy in weather & climate prediction, Journal of Computational Physics, 271, 2-18, doi:https://doi.org/10.1016/j.jcp.2013.10.042, 2014.

Düben, P. D. and Palmer, T. N.: Benchmark Tests for Numerical Weather Forecasts on Inexact Hardware, Monthly Weather Review, 142, 3809-3829, doi:https://doi.org/10.1175/MWR-D-14-00110.1, 2014.

Düben, P. D., Russell, F. P., Niu, X., Luk, W., and Palmer, T. N.: On the use of programmable hardware and reduced numerical precision in earth-system modeling, Journal of Advances in Modeling Earth Systems, 7, 1393-1408, doi:10.1002/2015MS000494, 2015.

Fornaciari, W., Agosta, G., Cattaneo, D., Denisov, L., Galimberti, A., Magnani, G., and Zoni, D.: Hardware and Software Support for Mixed Precision Computing: a Roadmap for Embedded and HPC Systems, 2023 Design, Automation & Test in Europe Conference & Exhibition (DATE), 2023, 1-6,

Fu, H., Liao, J., Ding, N., Duan, X., Gan, L., Liang, Y., Wang, X., Yang, J., Zheng, Y., Liu, W., Wang, L., and Yang, G.:
415   Redesigning CAM-SE for peta-scale climate modeling performance and ultra-high resolution on Sunway
        TaihuLight, Proceedings of the International Conference for High Performance Computing, Networking, Storage
        and Analysis, Denver, Colorado, 2017.

Fu, Z., Zhang, Y., Li, X., and Rong, X.: Intercomparison of Two Model Climates Simulated by a Unified Weather-
        Climate Model System (GRIST), Part I: Mean State, Climate Dynamics, 2024.

420   Gan, L., Fu, H., Luk, W., Yang, C., Xue, W., Huang, X., Zhang, Y., and Yang, G.: Accelerating solvers for global
        atmospheric equations through mixed-precision data flow engine, 2013 23rd International Conference on Field
        programmable Logic and Applications, 2013, 1-6,

Gu, J., Feng, J., Hao, X., Fang, T., Zhao, C., An, H., Chen, J., Xu, M., Li, J., Han, W., Yang, C., Li, F., and Chen, D.:
        Establishing a non-hydrostatic global atmospheric modeling system at 3-km horizontal resolution with aerosol
425   feedbacks on the Sunway supercomputer of China, Science Bulletin, doi:https://doi.org/10.1016/j.scib.2022.03.009,
        2022.

Harris, L. M. and Lin, S.-J.: A Two-Way Nested Global-Regional Dynamical Core on the Cubed-Sphere Grid, Monthly
        Weather Review, 141, 283-306, doi:10.1175/MWR-D-11-00201.1, 2012.

Jablonowski, C. and Williamson, D. L.: A baroclinic instability test case for atmospheric model dynamical cores,
430   Quarterly Journal of the Royal Meteorological Society, 132, 2943-2975, doi:10.1256/qj.06.12, 2006.

Jablonowski, C. and Williamson, D.: The Pros and Cons of Diffusion, Filters and Fixers in Atmospheric General
        Circulation Models, In: Lauritzen, P. H., C. Jablonowski, M. A. Taylor, R. D. Nair (Eds.), Numerical Techniques
        for Global Atmospheric Models, Lecture Notes in Computational Science and Engineering, Springer, Vol. 80, 381-
        493, 2011.

435   Klemp, J. B., Skamarock, W. C., and Park, S. H.: Idealized global nonhydrostatic atmospheric test cases on a reduced-
        radius sphere, Journal of Advances in Modeling Earth Systems, 7, 1155-1177, doi:10.1002/2015MS000435, 2015.

Li, J. and Zhang, Y.: Enhancing the stability of a global model by using an adaptively implicit vertical moist transport
        scheme, Meteorology and Atmospheric Physics, 134, 55, doi:10.1007/s00703-022-00895-5, 2022.

Li, X., Peng, X., and Zhang, Y.: Investigation of the effect of the time step on the physics–dynamics interaction in
440   CAM5 using an idealized tropical cyclone experiment, Climate Dynamics, 55, 665-680, doi:10.1007/s00382-020-
        05284-5, 2020.

Li, X., Zhang, Y., Peng, X., Zhou, B., Li, J., and Wang, Y.: Intercomparison of the weather and climate physics suites of
        a unified forecast–climate model system (GRIST-A22.7.28) based on single-column modeling, Geosci. Model Dev.,
        16, 2975-2993, doi:10.5194/gmd-16-2975-2023, 2023.

445   Maynard, C. M. and Walters, D. N.: Mixed-precision arithmetic in the ENDGame dynamical core of the Unified Model,
        a numerical weather prediction and climate model code, Computer Physics Communications, 244, 69-75,
        doi:https://doi.org/10.1016/j.cpc.2019.07.002, 2019.

Nakano, M., Yashiro, H., Kodama, C., and Tomita, H.: Single Precision in the Dynamical Core of a Nonhydrostatic Global Atmospheric Model: Evaluation Using a Baroclinic Wave Test Case, Monthly Weather Review, 146, 409-416, doi:10.1175/MWR-D-17-0257.1, 2018.

450

Palmer, T.: The ECMWF ensemble prediction system: Looking back (more than) 25 years and projecting forward 25 years, Quarterly Journal of the Royal Meteorological Society, 145, 12-24, doi:https://doi.org/10.1002/qj.3383, 2019.

Reed, K. A. and Jablonowski, C.: An Analytic Vortex Initialization Technique for Idealized Tropical Cyclone Studies in AGCMs, Monthly Weather Review, 139, 689-710, doi:10.1175/2010mwr3488.1, 2011.

455

Reed, K. A. and Jablonowski, C.: Idealized tropical cyclone simulations of intermediate complexity: A test case for AGCMs, Journal of Advances in Modeling Earth Systems, 4, doi:10.1029/2011MS000099, 2012.

Santos, F. F. D., Carro, L., Vella, F., and Rech, P.: Assessing the Impact of Compiler Optimizations on GPUs Reliability, ACM Trans. Archit. Code Optim., 21, Article 26, doi:10.1145/3638249, 2024.

460

Satoh, M., Tomita, H., Yashiro, H., Kajikawa, Y., Miyamoto, Y., Yamaura, T., Miyakawa, T., Nakano, M., Kodama, C., Noda, A. T., Nasuno, T., Yamada, Y., and Fukutomi, Y.: Outcomes and challenges of global high-resolution non-hydrostatic atmospheric simulations using the K computer, Progress in Earth and Planetary Science, 4, 13, doi:10.1186/s40645-017-0127-8, 2017.

Sergeev, D. E., Mayne, N. J., Bendall, T., Boutle, I. A., Brown, A., Kavčič, I., Kent, J., Kohary, K., Manners, J., Melvin,

465

T., Olivier, E., Ragta, L. K., Shipway, B., Wakelin, J., Wood, N., and Zerroukat, M.: Simulations of idealised 3D atmospheric flows on terrestrial planets using LFRic-Atmosphere, Geosci. Model Dev., 16, 5601-5626, doi:10.5194/gmd-16-5601-2023, 2023.

Skamarock, W. C., Klemp, J. B., Duda, M. G., Fowler, L. D., Park, S.-H., and Ringler, T. D.: A Multiscale Nonhydrostatic Atmospheric Model Using Centroidal Voronoi Tesselations and C-Grid Staggering, Monthly

470

Weather Review, 140, 3090-3105, doi:10.1175/MWR-D-11-00215.1, 2012.

Stevens, B., Satoh, M., Auger, L., Biercamp, J., Bretherton, C. S., Chen, X., Düben, P., Judt, F., Khairoutdinov, M., Klocke, D., Kodama, C., Kornblueh, L., Lin, S.-J., Neumann, P., Putman, W. M., Röber, N., Shibuya, R., Vanniere, B., Vidale, P. L., Wedi, N., and Zhou, L.: DYAMOND: the DYnamics of the Atmospheric general circulation Modeled On Non-hydrostatic Domains, Progress in Earth and Planetary Science, 6, 61, doi:10.1186/s40645-019-

475

0304-z, 2019.

Taylor, M., Caldwell, P. M., Bertagna, L., Clevenger, C., Donahue, A., Foucar, J., Guba, O., Hillman, B., Keen, N., Krishna, J., Norman, M., Sreepathi, S., Terai, C., White, J. B., Salinger, A. G., McCoy, R. B., Leung, L.-y. R., Bader, D. C., and Wu, D.: The Simple Cloud-Resolving E3SM Atmosphere Model Running on the Frontier Exascale System, Proceedings of the International Conference for High Performance Computing, Networking,

480

Storage and Analysis, <conf-loc>, <city>Denver</city>, <state>CO</state>, <country>USA</country>, </conf-loc>, 2023.

Thornes, T., Düben, P., and Palmer, T.: On the use of scale-dependent precision in Earth System modelling, Quarterly Journal of the Royal Meteorological Society, 143, 897-908, doi:https://doi.org/10.1002/qj.2974, 2017.

Thuburn, J.: Some conservation issues for the dynamical cores of NWP and climate models, Journal of Computational Physics, 227, 3715-3730, doi:http://dx.doi.org/10.1016/j.jcp.2006.08.016, 2008.

Tomita, H. and Satoh, M.: A new dynamical framework of nonhydrostatic global model using the icosahedral grid, Fluid Dynamics Research, 34, 357, 2004.

Ullrich, P. A., Melvin, T., Jablonowski, C., and Staniforth, A.: A proposed baroclinic wave test case for deep- and shallow-atmosphere dynamical cores, Quarterly Journal of the Royal Meteorological Society, 140, 1590-1602, doi:10.1002/qj.2241, 2014.

Váňa, F., Düben, P., Lang, S., Palmer, T., Leutbecher, M., Salmond, D., and Carver, G.: Single Precision in Weather Forecasting Models: An Evaluation with the IFS, Monthly Weather Review, 145, 495-502, doi:10.1175/MWR-D-16-0228.1, 2016.

Wedi, N. P. and Smolarkiewicz, P. K.: A framework for testing global non-hydrostatic models, Quarterly Journal of the Royal Meteorological Society, 135, 469-484, doi:10.1002/qj.377, 2009.

Wedi, N. P., Polichtchouk, I., Dueben, P., Anantharaj, V. G., Bauer, P., Boussetta, S., Browne, P., Deconinck, W., Gaudin, W., Hadade, I., Hatfield, S., Iffrig, O., Lopez, P., Maciel, P., Mueller, A., Saarinen, S., Sandu, I., Quintino, T., and Vitart, F.: A Baseline for Global Weather and Climate Simulations at 1 km Resolution, Journal of Advances in Modeling Earth Systems, 12, e2020MS002192, doi:https://doi.org/10.1029/2020MS002192, 2020.

Yang, C., Xue, W., Fu, H., You, H., Wang, X., Ao, Y., Liu, F., Gan, L., Xu, P., Wang, L., Yang, G., and Zheng, W.: 10M-Core Scalable Fully-Implicit Solver for Nonhydrostatic Atmospheric Dynamics, SC '16: Proceedings of the International Conference for High Performance Computing, Networking, Storage and Analysis, 2016, 57-68,

Yin, F., Song, J., Wu, J., and Zhang, W.: An implementation of single-precision fast spherical harmonic transform in Yin–He global spectral model, Quarterly Journal of the Royal Meteorological Society, 147, 2323-2334, doi:https://doi.org/10.1002/qj.4026, 2021.

Yu, R., Zhang, Y., Wang, J., Li, J., Chen, H., Gong, J., and Chen, J.: Recent Progress in Numerical Atmospheric Modeling in China, Advances in Atmospheric Sciences, 36, 938-960, doi:10.1007/s00376-019-8203-1, 2019.

Zängl, G., Reinert, D., Rípodas, P., and Baldauf, M.: The ICON (ICOsahedral Non-hydrostatic) modelling framework of DWD and MPI-M: Description of the non-hydrostatic dynamical core, Quarterly Journal of the Royal Meteorological Society, 141, 563-579, doi:10.1002/qj.2378, 2015.

Zarzycki, C. M., Jablonowski, C., Kent, J., Lauritzen, P. H., Nair, R., Reed, K. A., Ullrich, P. A., Hall, D. M., Taylor, M. A., Dazlich, D., Heikes, R., Konor, C., Randall, D., Chen, X., Harris, L., Giorgetta, M., Reinert, D., Kühnlein, C., Walko, R., Lee, V., Qaddouri, A., Tanguay, M., Miura, H., Ohno, T., Yoshida, R., Park, S. H., Klemp, J. B., and Skamarock, W. C.: DCMIP2016: the splitting supercell test case, Geosci. Model Dev., 12, 879-892, doi:10.5194/gmd-12-879-2019, 2019.

Zhang, Y. and Chen, H.: Comparing CAM5 and Superparameterized CAM5 Simulations of Summer Precipitation Characteristics over Continental East Asia: Mean State, Frequency?Intensity Relationship, Diurnal Cycle, and Influencing Factors, Journal of Climate, 29, 1067-1089, doi:10.1175/JCLI-D-15-0342.1, 2016.

Zhang, Y.: Extending High-Order Flux Operators on Spherical Icosahedral Grids and Their Applications in the Framework of a Shallow Water Model, Journal of Advances in Modeling Earth Systems, 10, 145-164, doi:10.1002/2017MS001088, 2018.

Zhang, Y., Li, J., Yu, R., Zhang, S., Liu, Z., Huang, J., and Zhou, Y.: A Layer-Averaged Nonhydrostatic Dynamical Framework on an Unstructured Mesh for Global and Regional Atmospheric Modeling: Model Description, Baseline Evaluation, and Sensitivity Exploration, Journal of Advances in Modeling Earth Systems, 11, 1685-1714, doi:10.1029/2018MS001539, 2019.

Zhang, Y., Li, J., Yu, R., Liu, Z., Zhou, Y., Li, X., and Huang, X.: A Multiscale Dynamical Model in a Dry-Mass Coordinate for Weather and Climate Modeling: Moist Dynamics and Its Coupling to Physics, Monthly Weather Review, 148, 2671-2699, doi:10.1175/MWR-D-19-0305.1, 2020.

Zhang, Y., Yu, R., Li, J., Li, X., Rong, X., Peng, X., and Zhou, Y.: AMIP Simulations of a Global Model for Unified Weather-Climate Forecast: Understanding Precipitation Characteristics and Sensitivity Over East Asia, Journal of Advances in Modeling Earth Systems, 13, e2021MS002592, doi:https://doi.org/10.1029/2021MS002592, 2021.

Zhang, Y., Li, X., Liu, Z., Rong, X., Li, J., Zhou, Y., and Chen, S.: Resolution Sensitivity of the GRIST Nonhydrostatic Model From 120 to 5 km (3.75 km) During the DYAMOND Winter, Earth and Space Science, 9, e2022EA002401, doi:https://doi.org/10.1029/2022EA002401, 2022.

Zhang, Y., Li, J., Zhang, H., Li, X., Dong, L., Rong, X., Zhao, C., Peng, X., and Wang, Y.: History and Status of Atmospheric Dynamical Core Model Development in China, in: Numerical Weather Prediction: East Asian Perspectives, edited by: Park, S. K., Springer International Publishing, Cham, 3-36, 2023.

540

Table 1. Grid Name and Corresponding Horizontal Resolutions.

Grid Name	Horizontal Resolution	Number of Cells
G6	120km	40,962
G7	60km	163,842
G8	30km	655,362
G9B3	5km	23,592,962

Table 2. Elapsed time using single-, mixed- and double precision **(The runtime of each solver is normalized to that of the corresponding solver in double-precision).**

Grid Name	Precision	Dycore time (1440step)	Tracer time (1440step)
G8	DBL	1 (NDC) 1 (HDC)	1
	SGL	0.53 (NDC) 0.56 (HDC)	0.58
	MIX	0.73 (NDC) 0.76 (HDC)	0.56

545
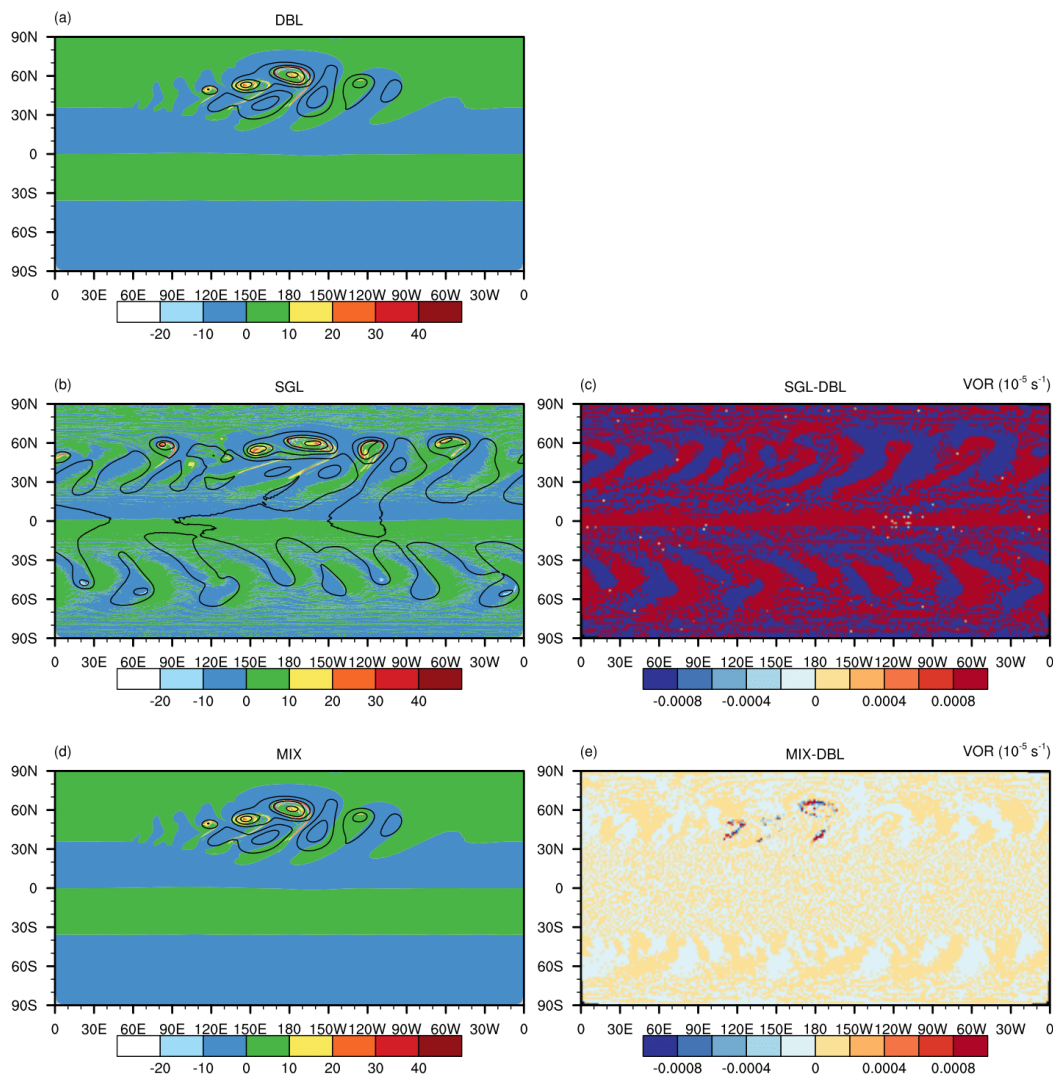
Figure 1: Baroclinic wave development at day 11 in the (a) DBL simulation, (b) SGL simulation and (d) MIX simulation. (left) Colors show relative vorticity ($\times 10^{-5}\ s^{-1}$) and contours of the surface pressure and (right) the difference between SGL and DBL, as well as the difference between MIX and DBL.
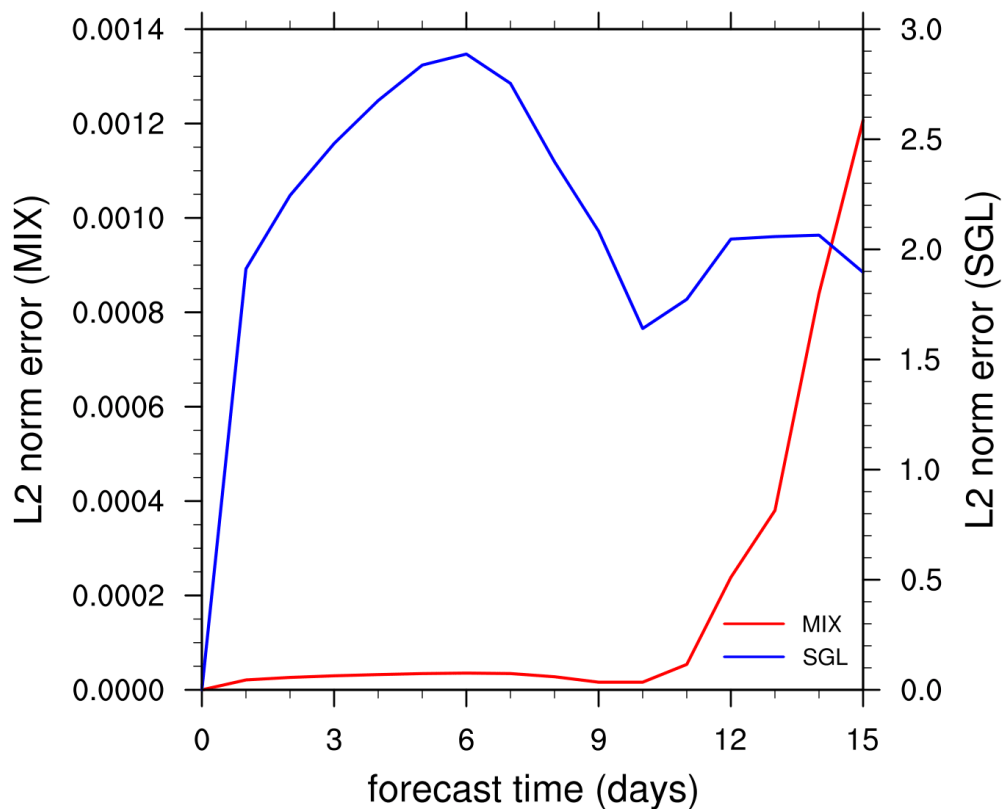
Figure 2: Time evolution of global l_2 difference norm of simulated relative vorticity between the SGL and DBL, as well as l_2 difference norm between the MIX and DBL. Red and blue represent SGL and MIX experiments, respectively.
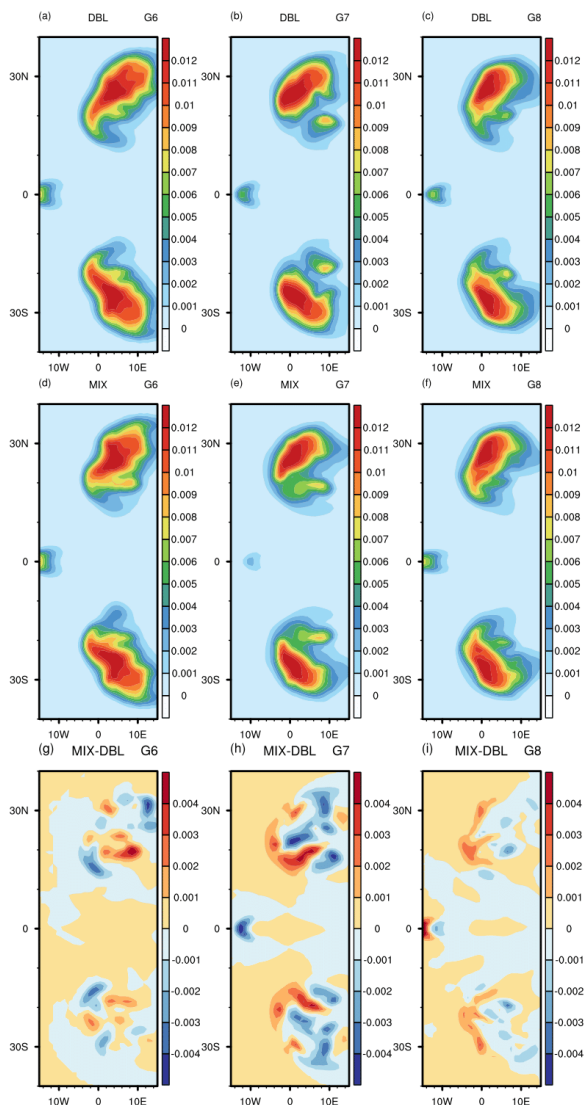
Figure 3: Rainwater mixing ratios at the three horizontal resolutions: (left to right) G6, G7 and G8. Result using (top to bottom) DBL, MIX and the difference between MIX and DBL.
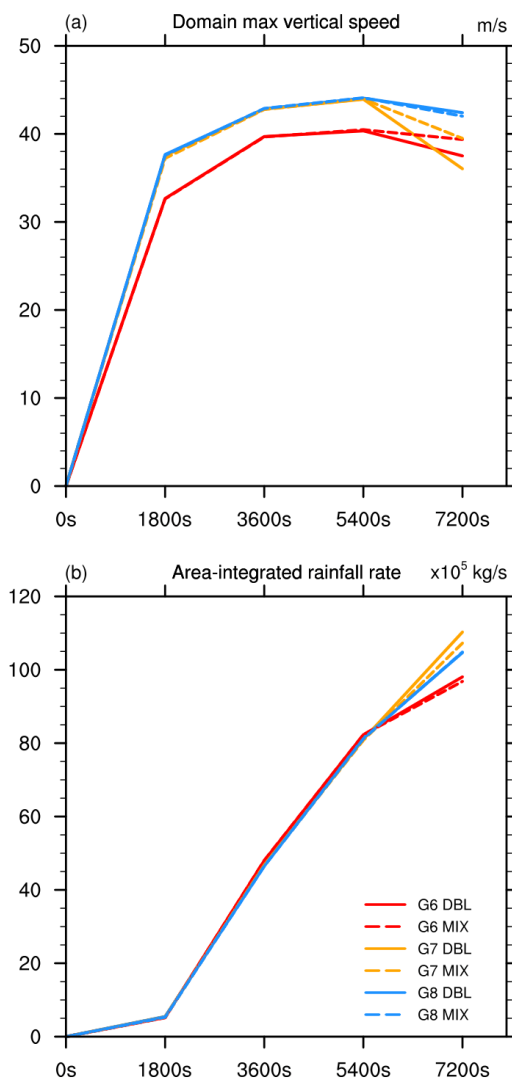
Figure 4: The (a) domain maximum vertical speed and (b) area-integrated rainfall rate obtained from the supercell simulations.

565
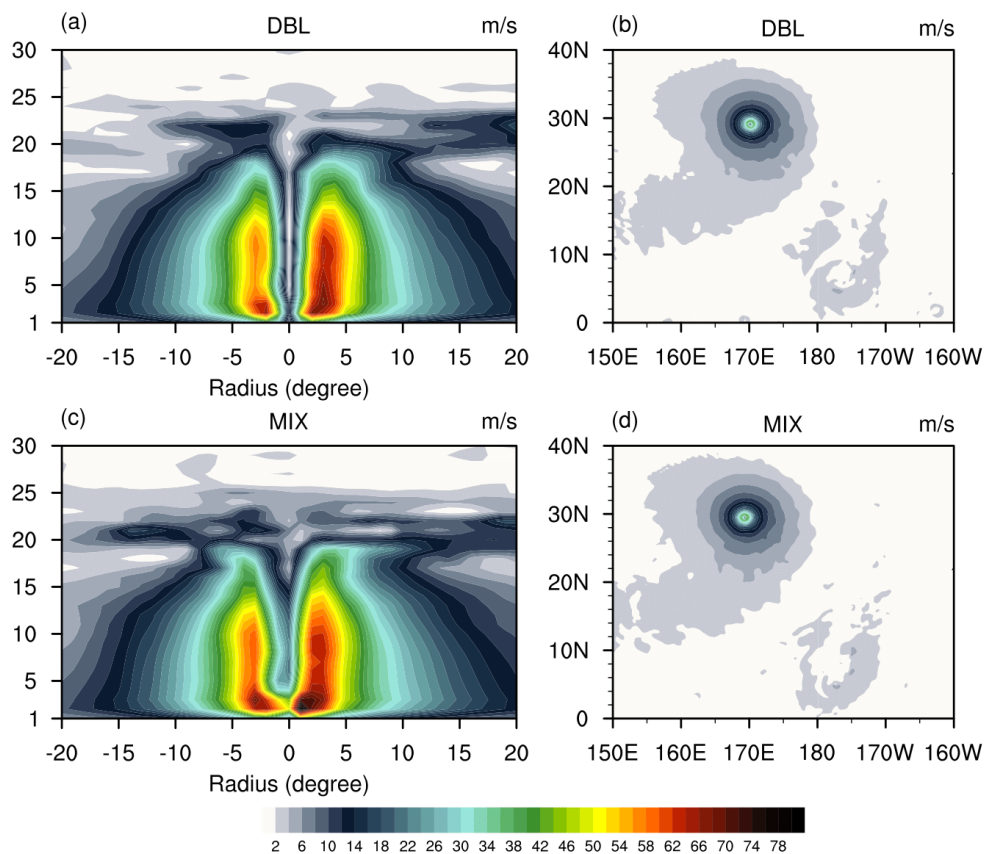
Figure 5: The simulated wind speed (m s⁻¹) at the G8 resolution with NDC solver, including MIX (a, b) and DBL (c, d) simulations. (left) Longitude-height cross section of the wind speed through the center latitude of the vortex as a function of the radius from the vortex center. (right) Horizontal cross section of the wind speed at surface model layer.
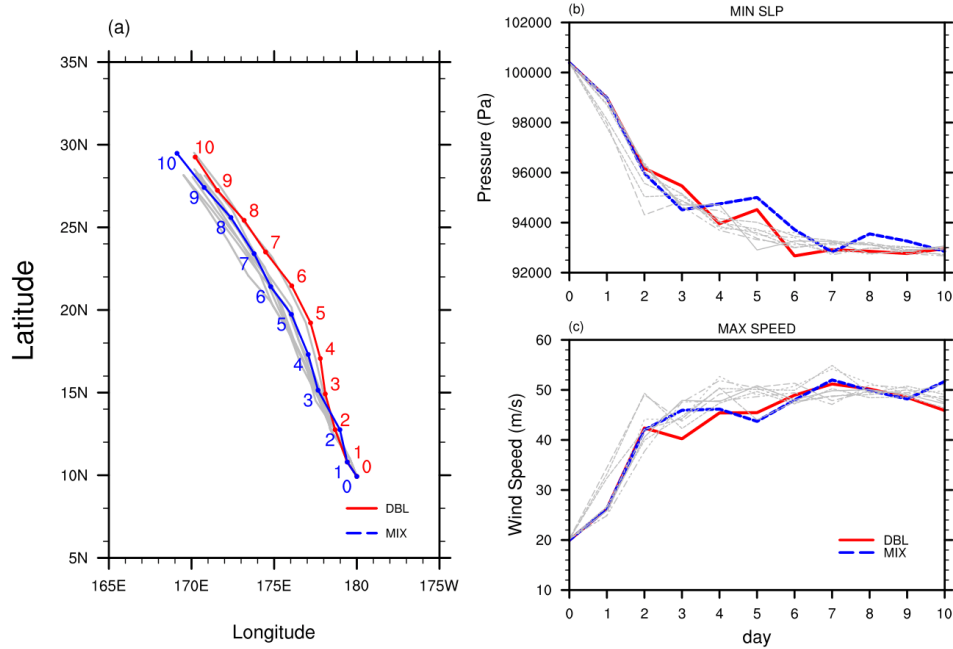
Figure 6: The results of deterministic and ensemble simulations. (a) The track of the tropical cyclone center for MIX (blue lines) and DBL (read lines) deterministic simulations. Time evolution of the (b) minimum surface pressure and (c) maximum surface wind speed from the and deterministic and ensemble simulations. The red and blue lines represent the deterministic MIX and DBL simulations, respectively. The gray lines represent the eight runs with random perturbations to initial normal velocity at cell edges.

575
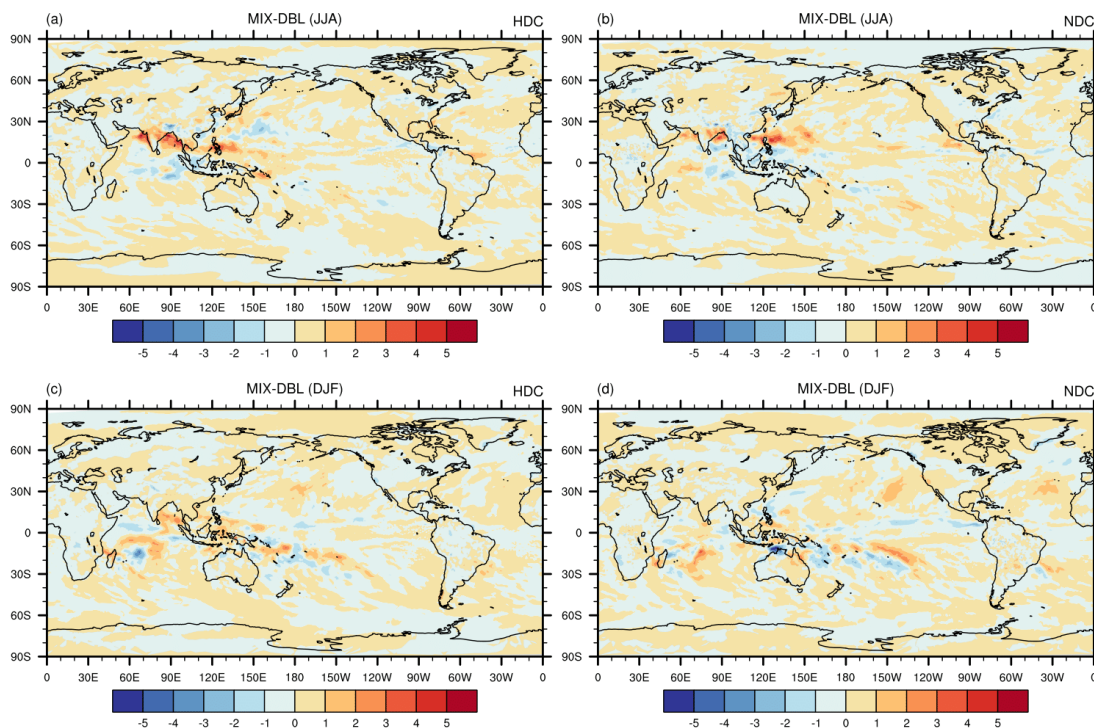
Figure 7: The difference between the MIX and DBL simulations, including solutions from the hydrostatic (left column) and non-hydrostatic (right column) solver. The first and second rows respectively display the averaged (2001-2010) precipitation rate (mm/day) for JJA and DJF.
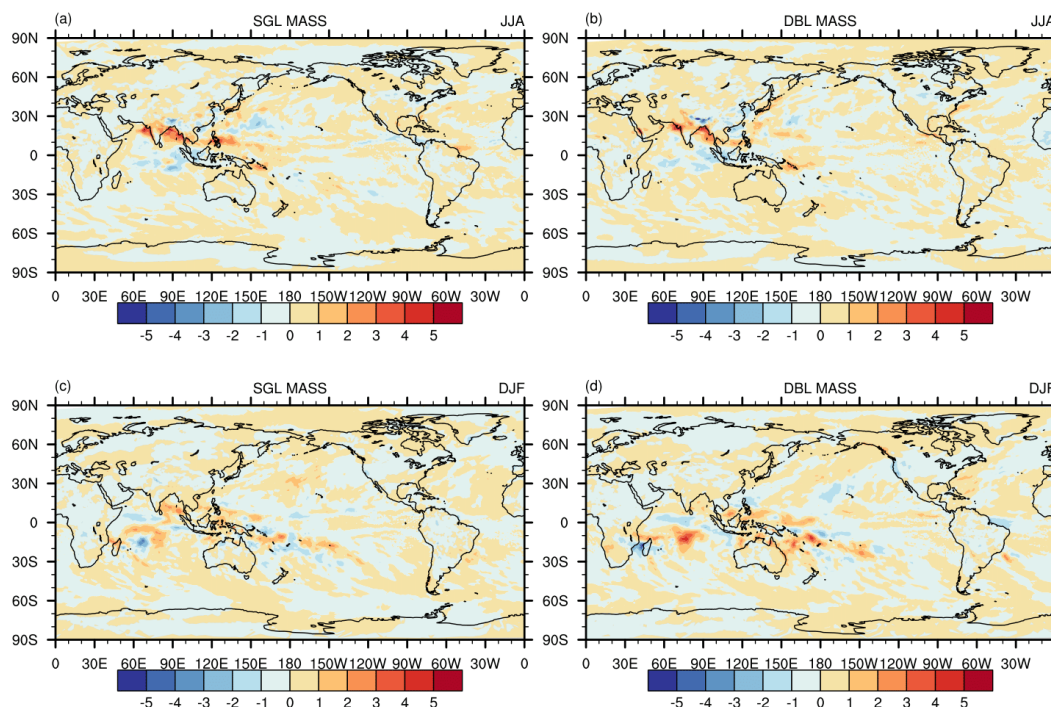
585

Figure 8: (a) Difference between the JJA-averaged (2001-2010) precipitation rate (mm/day) simulated by the SGL continuous equation solver in mixed-precision mode and the "true value"; (b) same as (a) but for the DBL continuous equation solver. (c)-(d) same as (a)-(b) but for the DJF-averaged (2001-2010) results.

590
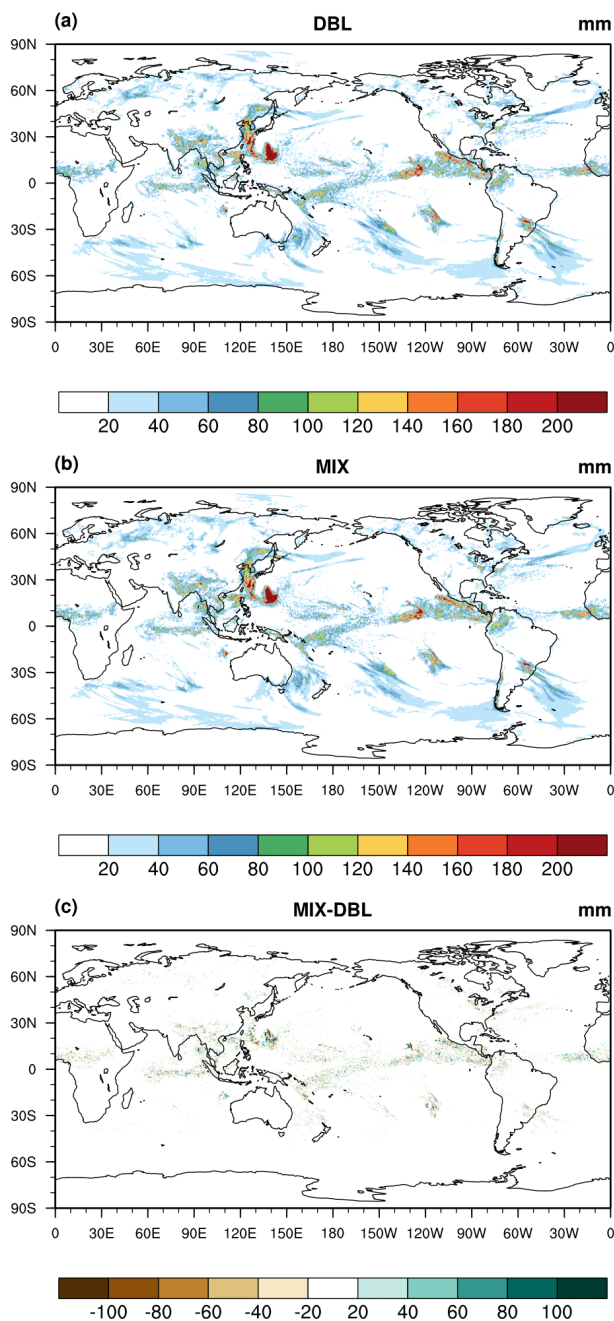
Figure 9: The 5-day (from 0000 UTC on 10 to 0000 UTC on 15 July 2015) accumulated precipitation (units: mm) from the (a) DBL simulation, (b) MIX simulation and (c) the difference between MIX and DBL simulations.